

1    **Different physicochemical behaviors of nitrate and ammonium**  
2    **during transport: a case study on Mt. Hua, China**

3  
4    Can Wu<sup>1</sup>, Cong Cao<sup>2,a</sup>, Jianjun Li<sup>2</sup>, Shaojun Lv<sup>1</sup>, Jin Li<sup>2,b</sup>, Xiaodi Liu<sup>1</sup>, Si Zhang<sup>1</sup>,  
5    Shijie Liu<sup>1</sup>, Fan Zhang<sup>1</sup>, Jingjing Meng<sup>4</sup>, Gehui Wang<sup>1,3\*</sup>

6  
7  
8    <sup>1</sup> Key Lab of Geographic Information Science of the Ministry of Education, School of  
9    Geographic Sciences, East China Normal University, Shanghai 200062, China

10  
11    <sup>2</sup> State Key Laboratory of Loess and Quaternary Geology, Institute of Earth  
12    Environment, Chinese Academy of Sciences, Xi'an 710061, China

13    <sup>3</sup> Institute of Eco-Chongming, Chenjia Zhen, Chongming, Shanghai 202162, China

14    <sup>4</sup> School of Environment and Planning, Liaocheng University, Liaocheng 252000,  
15    China

16  
17    <sup>a</sup> Now at The State University of New York at Stony Brook.

18    <sup>b</sup> Now at Institute for Environmental and Climate Research, Jinan University.

19  
20  
21  
22  
23  
24    \*Corresponding author. Gehui Wang ([ghwang@geo.ecnu.edu.cn](mailto:ghwang@geo.ecnu.edu.cn))

36 **Abstract:** To understand the chemical evolution of aerosols in the transport process,  
37 the chemistry of PM<sub>2.5</sub> and nitrogen isotope compositions on the mountainside of Mt.  
38 Hua (~1120 m a.s.l.) in inland China during the 2016 summertime were investigated  
39 and compared with parallel observations collected at surface sampling site (~400 m  
40 a.s.l.). PM<sub>2.5</sub> exhibited a high level at the mountain foot site (MF) (aver. 76.0±44.1  
41 µg/m<sup>3</sup>) and could be transported aloft by anabatic valley winds, leading to the gradual  
42 accumulation of daytime PM<sub>2.5</sub> with a noon peak at the mountainside sampling site  
43 (MS). As the predominant ion species, sulfate exhibited nearly identical mass  
44 concentrations in both sites, but its PM<sub>2.5</sub> mass fraction was moderately enhanced by  
45 ~4% at the MS site. The ammonium variations were similar to the sulfate variations,  
46 the chemical forms of both of which mainly existed as ammonium bisulfate (NH<sub>4</sub>HSO<sub>4</sub>)  
47 and ammonium sulfate ((NH<sub>4</sub>)<sub>2</sub>SO<sub>4</sub>) at the MF and MS sites, respectively. Unlike  
48 sulfate and ammonium, nitrate mainly existed as ammonium nitrate (NH<sub>4</sub>NO<sub>3</sub>) in fine  
49 particles and exhibited decreasing mass concentration and proportion trends with  
50 increasing elevation. This finding was ascribed to NH<sub>4</sub>NO<sub>3</sub> volatilization, in which  
51 gaseous HNO<sub>3</sub> from semi-volatile NH<sub>4</sub>NO<sub>3</sub> subsequently reacted with dust particles to  
52 form nonvolatile salts, resulting in significant nitrate shifts from fine particles into  
53 coarse particles. Such scavenging of fine-particle nitrate led to an enrichment in the  
54 daytime <sup>15</sup>N of nitrate at the MS site compared with to the MF site. In contrast to nitrate,  
55 at the MS site, the <sup>15</sup>N in ammonium depleted during the daytime. Considering the lack  
56 of any significant change in ammonia (NH<sub>3</sub>) sources during the vertical transport  
57 process, this <sup>15</sup>N depletion in ammonium was mainly the result of unidirectional

58 reactions, indicating that additional NH<sub>3</sub> would partition into particulate phases and  
59 further neutralize HSO<sub>4</sub><sup>-</sup> to form SO<sub>4</sub><sup>2-</sup>. This process would reduce the aerosol acidity,  
60 with a higher pH (3.4±2.2) at MS site and lower ones (2.9±2.0) at MF site. Our work  
61 provides more insight into physicochemical behaviors of semi-volatile nitrate and  
62 ammonium, which will facilitate the improvement in model for a better simulation of  
63 aerosol composition and properties.

64 **Keywords:** Ammonium; Nitrate; Stable nitrogen isotope; Haze; Volatilization

65

66

67

68

69

70

71

72

73

74

75

76

77

78

79

80 **1 Introduction**

81 Atmospheric particulate matter measuring equal to or less than 2.5  $\mu\text{m}$  in  
82 aerodynamic diameter (PM<sub>2.5</sub>) is a worldwide air pollution burden that can deteriorate  
83 the urban air quality and induce adverse human health effects that contribute to  
84 lowering life expectancies (Shiraiwa et al., 2017; Lelieveld et al., 2015; Fuzzi et al.,  
85 2015; Wang et al., 2016). Recent studies have disclosed that the mechanisms underlying  
86 these effects are profoundly dependent on particle properties, e.g., the size,  
87 concentration, mixing state and chemical compositions of particles (Li et al., 2016; Liu  
88 et al., 2021; Guo et al., 2014). Thus, since 2013, China has issued strict emission  
89 directives to mitigate haze pollution. Consequently, the annual PM<sub>2.5</sub> concentration in  
90 China fell by approximately one-third from 2013–2017 (Zheng et al., 2018).  
91 Notwithstanding, the PM<sub>2.5</sub> levels in most cities in China still exceed the least-stringent  
92 target of the World Health Organization (WHO 2021; 35  $\mu\text{g}/\text{m}^3$ ), especially in rural  
93 areas and small cities (Lv et al., 2022; Li et al., 2023).

94 Near-surface PM can also be transported to the upper air, and this process critically  
95 impacts radiative forcing, cloud precipitation and the regional climate by  
96 scattering/absorbing solar radiation and by influencing aerosol-cloud interactions (Van  
97 Donkelaar et al., 2016; Andreae and Ramanathan, 2013; Fan et al., 2018). Past  
98 assessments of these effects have been characterized by large uncertainties (Carslaw et  
99 al., 2013); for example, Bond et al. (2013) found that black carbon climate forcing  
100 varied from +0.17  $\text{W}/\text{m}^2$  to +2.1  $\text{W}/\text{m}^2$  with a 90% uncertainty. Such massive  
101 uncertainties are mainly due to our limited knowledge regarding the spatiotemporal

102 distribution, abundance and compositions of airborne PM (Seinfeld and Johnh, 2016;  
103 Raes et al., 2000). In addition, aerosols may undergo aging during the vertical transport  
104 process, causing increasingly complex compositions and changes in aerosol properties.

105 Despite these factors, to date, vertical observations remain comparatively scarce  
106 compared to surface measurements. Therefore, to obtain an improved understanding of  
107 the fundamental chemical and dynamical processes governing haze development, more  
108 field observations of upper-layer aerosols are necessary, as these measurements could  
109 provide updated kinetic and mechanistic parameters that could serve to improve model  
110 simulations.

111 Currently, various monitoring approaches have been developed and applied to  
112 measure vertical aerosols, e.g., satellite remote sensing and in situ lidar methods; these  
113 approaches can be used to obtain the pollution concentration profiles (Van Donkelaar  
114 et al., 2016; Reid et al., 2017). To accurately measure chemical compositions, aircraft  
115 and unmanned aerial vehicles (UAVs) equipped with a variety of instruments can be  
116 utilized in short-term sampling campaigns (Lambey and Prasad, 2021; Zhang et al.,  
117 2017), but these tools are unsuitable for long-term continued observations due to their  
118 high operational costs. In cases of near-surface vertical urban atmosphere observations,  
119 techniques involving tethered balloons, meteorological towers and skyscrapers are  
120 usually adopted (Zhou et al., 2020; Xu et al., 2018; Fan et al., 2021). However, the  
121 vertical application range of these methods are limited to only ~500 m, thus hardly  
122 meeting the requirements of research conducted above the boundary layer. Therefore,  
123 high-elevation mountain sites have long been regarded as suitable places for long-term

124 research on the upper-layer aerosol (including its compositions, chemical-physical  
125 properties and formation processes, etc.) (Dzepina et al., 2015; Zhou et al., 2021; Wang  
126 et al., 2013), which are conducive to better understanding of the haze episodes in the  
127 lower troposphere. Although the fixed observation position is the key drawback of this  
128 monitoring approach, it has still been widely selected for use in various vertical  
129 observation campaigns, e.g., in past studies conducted in Salt Lake Valley (Baasandorj  
130 et al., 2017), in Terni Valley (Ferrero et al., 2012) and on Mt. Tai (Meng et al., 2018;  
131 Wang et al., 2011).

132 Mt. Hua adjoins the Guanzhong Basin of inland China, where haze pollution has  
133 been a persistent environmental problem (Wu et al., 2020b; Wu et al., 2021; Wang et  
134 al., 2016). In our previous studies conducted at the mountaintop of Mt. Hua, we found  
135 that air quality was significantly affected by surface pollution, and distinctive  
136 differences were found in the aerosol compositions and size distributions at the  
137 mountaintop compared to those measured at lower elevations ground level (Wang et al.,  
138 2013; Li et al., 2013). With the implementation of strict emission controls, the  
139 atmospheric environment in this region has changed dramatically from the SO<sub>2</sub>/sulfate-  
140 dominated previous environment to the current NO<sub>x</sub>/nitrate-dominated environment  
141 (Baasandorj et al., 2017; Wu et al., 2020c). However, the fundamental chemical and  
142 dynamical processes driving this PM<sub>2.5</sub>-loading explosion are unclear under the current  
143 atmospheric state with increasing O<sub>3</sub> and NH<sub>3</sub> levels. To better rationalize these  
144 processes, in this work, 4-hr integrated aerosol samples were synchronously collected  
145 on the mountainside and at the lower-elevation land surface, and the chemical

146 components and stable nitrogen isotope compositions of nitrate and ammonium were  
147 analyzed in the collected PM<sub>2.5</sub> samples. We compared the chemical compositions and  
148 diurnal cycles between the two sampling sites and then discussed the changes in the  
149 chemical forms of secondary inorganic ions during their vertical transport from lower  
150 to higher elevations. Our study revealed that nitrate and ammonium exhibited distinct  
151 physicochemical behaviors during the aerosol-aging process.

152 **2 Experiment**

153 **2.1 Sample collection**

154 In this campaign, the PM<sub>2.5</sub> samples were synchronously collected at two locations  
155 in the Mt. Hua area during the period from 27 August to 17 September 2016. One  
156 sampling site was located on a building belonging to the Huashan Meteorological  
157 Bureau (34°32'N, 110°5'E, 400 m a.s.l.) at the foot of Mt. Hua. Surrounded by several  
158 traffic arteries and dense residential and commercial buildings, as shown in Figure 1b,  
159 this site is an ideal urban station for studying the impacts of anthropogenic activities on  
160 local air quality and is referred to hereafter as the “MF” site. The mountainous sampling  
161 site (34°29'N, 110°3'E, 1120 m a.s.l.) was located approximately 8 km from the city  
162 site horizontally (Figure 1c) at an elevation of 720 m above the average Huashan town  
163 level of ~400 m (a.s.l.). This site was situated on a mountainside that experiences little  
164 anthropogenic activity due to its steep terrain and is abbreviated hereafter as the “MS”  
165 site. Furthermore, this location adjoins one of the larger valleys of Mt. Hua; therefore,  
166 the measurements taken at this location were strongly affected by the lower-elevation  
167 air pollutants transported upwards by the valley winds. At both measurement sites, the

168 PM<sub>2.5</sub> aerosol samples with a 4-hr interval in were collected onto prebaked (at 450°C  
169 for 6 hrs) quartz filters using high-volume (1.13-m<sup>3</sup>/min) air samplers (Tisch  
170 Environmental, Inc., USA). All air samplers were installed on the roofs of buildings,  
171 approximately 15 m above the local ground surface. Furthermore, size-resolved aerosol  
172 sampling was synchronously conducted at two sites during summertime (10-22 August,  
173 2020); and these samples with nine size bins (cutoff points were 0.43, 0.65, 1.1, 2.1,  
174 3.3, 4.7, 5.8 and 9.0  $\mu\text{m}$ , respectively) were collected using an Anderson sampler at an  
175 airflow rate of 28.3 L/min for ~72 h. After sampling, the filter samples were stored in a  
176 freezer (at -18°C) prior to analysis.

177 The hourly PM<sub>2.5</sub>, NO<sub>x</sub> and O<sub>3</sub> mass concentrations were detected at the  
178 mountainside sampling site using an E-BAM, a chemiluminescence analyzer (Thermo,  
179 Model 42i, USA) and a UV photometric analyzer (Thermo, Model 49i, USA),  
180 respectively. At the MF site, only PM<sub>2.5</sub> was monitored, using another E-BAM, while  
181 the data of the other species were downloaded from the Weinan Ecological  
182 Environment Bureau (<http://sthjj.weinan.gov.cn/>). Meteorological data characterizing  
183 both sampling sites throughout the whole campaign were obtained from the Shaanxi  
184 Meteorological Bureau website (<http://sn.cma.gov.cn/>).

185 **2.2 Chemical analysis**

186 Four punches (1.5-cm diameter) of each aerosol sample were extracted into 10-mL  
187 Milli-Q pure water (18.2 MΩ) under sonication for 30 min. Subsequently, the extracts  
188 were filtered with 0.45- $\mu\text{m}$  syringe filters and detected for water-soluble ions (Na<sup>+</sup>,  
189 NH<sub>4</sub><sup>+</sup>, K<sup>+</sup>, Mg<sup>2+</sup>, Ca<sup>2+</sup>, SO<sub>4</sub><sup>2-</sup>, NO<sub>2</sub><sup>-</sup>, NO<sub>3</sub><sup>-</sup> and Cl<sup>-</sup>) by using ion chromatography; the

190 detection limit for these nine ions was < 0.01  $\mu\text{g}/\text{mL}$ . A DRI-model 2001 thermal–  
191 optical carbon analyzer was used herein following the IMPROVE-A protocol to analyze  
192 the organic carbon (OC) and elemental carbon (EC) in each  $\text{PM}_{2.5}$  filter sample (in  
193  $0.526 \text{ cm}^2$  punches). For more details regarding the utilized methods, readers can refer  
194 to our previous studies (Wu et al., 2020b).

195 To quantify the stable nitrogen isotope compositions of nitrate ( $\delta^{15}\text{N-NO}_3^-$ ) and  
196 ammonium ( $\delta^{15}\text{N-NH}_4^+$ ) in  $\text{PM}_{2.5}$  samples, the filter samples were pretreated as  
197 described for the water-soluble ion analysis. The ammonium in the extracts  
198 (approximately half of the resulting solution) was oxidized by hypobromite ( $\text{BrO}^-$ ) to  
199 nitrite ( $\text{NO}_2^-$ ), which was subsequently reduced by hydroxylamine ( $\text{NH}_2\text{OH}$ ) in a  
200 strongly acidic environment. The above product ( $\text{N}_2\text{O}$ ) was then analyzed by a  
201 commercially available purge and cryogenic trap system coupled to an isotope ratio  
202 mass spectrometer (PT-IRMS). A bacterial method (*Pseudomonas aureofaciens*, a  
203 denitrifying bacterium without  $\text{N}_2\text{O}$  reductase activity) was used herein to convert the  
204 sample  $\text{NO}_3^-$  into  $\text{N}_2\text{O}$ , which was ultimately quantified through PT-IRMS. As revealed  
205 in previous studies (Fang et al., 2011), the presence of  $\text{NO}_2^-$  in aerosols may interfere  
206 with the denitrifier method when measuring  $\delta^{15}\text{N}$ . Nonetheless,  $\text{NO}_2^-$  generally  
207 composed tiny portions in most of our samples and, on average, contributed <1.0% to  
208  $\text{NO}_3^- + \text{NO}_2^-$ . Thus, we believed that the proportion of  $\text{NO}_2^-$  in the sample was too small  
209 to affect the resulting  $\delta^{15}\text{N}$  measurements based on the discussions reported by Wankel  
210 et al. (2010). More details regarding the analytical artifact and quality control protocols  
211 can be found elsewhere (Wu et al., 2021; Liu et al., 2014).

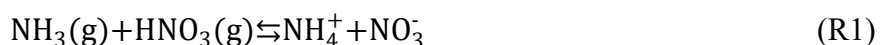
212 **2.3 Concentration-weighted trajectory (CWT) analysis**

213 CWT is a powerful tool used herein to reveal the potential spatial sources responsible  
214 for the high PM<sub>2.5</sub> loadings measured on Mt. Hua; this method has been used previously  
215 in similar studies (Wu et al., 2020c; Wu et al., 2020a). In this study, the CWT analysis  
216 was conducted using the Igor-based tool coupled with hourly PM<sub>2.5</sub> concentrations and  
217 12-hr air mass backward trajectories that were simulated by using the Hybrid-Single  
218 Particle Lagrangian Integrated Trajectory (HYSPPLIT) model (Petit et al., 2017).

219 **2.4 Theoretical calculations of the partial pressures of NH<sub>3</sub> and HNO<sub>3</sub> and the  
220 dissociation constant of NH<sub>4</sub>NO<sub>3</sub>**

221 To obtain the product of the partial pressures of NH<sub>3</sub> and HNO<sub>3</sub>, the NH<sub>4</sub>NO<sub>3</sub>  
222 deliquescence relative humidity (DRH) was first calculated using equation (1) (Eq. 1).  
223 The average DRH of NH<sub>4</sub>NO<sub>3</sub> between the two sites was 65.0±2.9%, slightly lower  
224 than the atmospheric RH (66.0±19.3%). As the works by Wexler and Seinfeld (1991)  
225 and Tang and Munkelwitz (1993) revealed, aerosols are multicomponent mixtures, and  
226 which the aerosol DRH is always lower than the DRH of the individual salts in the  
227 particles. Thus, the actual DRH of the aerosols observed in this study would be lower  
228 than the calculated DRH of NH<sub>4</sub>NO<sub>3</sub>. Based on these analyses, the particles would be  
229 deliquescent most of the time, but for simplification, we always assumed that NH<sub>4</sub>NO<sub>3</sub>  
230 was in an aqueous state, corresponding to the following dissociation reaction (R1):

$$\ln(\text{DRH}) = \frac{723.7}{T} + 1.6954 \quad (\text{Eq. 1})$$



231 According to the approach illustrated in the referenced work (Seinfeld and Johnh,

232 2016), the equilibrium constant of the dissociation reaction can be described as the  
233 equation (2).

$$K_{AN} = \frac{\gamma_{NH_4NO_3}^2 m_{NH_4^+} m_{NO_3^-}}{p_{HNO_3} p_{NH_3}} \quad (Eq. 2)$$

$$K_{AN} = 4 \times 10^{17} \exp \left\{ 64.7 \left( \frac{298}{T} - 1 \right) + 11.51 \left[ 1 + \ln \left( \frac{298}{T} \right) - \frac{298}{T} \right] \right\} \quad (Eq. 3)$$

$$\ln(K_p) = 118.7 - \frac{24084}{T} - 6.025 \ln(T) \quad (Eq. 4)$$

234 where  $K_{AN}$  ( $\text{mol}^2/(\text{kg}^2 \text{ atm}^2)$ ) is the equilibrium constant of R1 (this value is  
235 temperature-dependent and can be calculated by Eq. 3),  $\gamma_{NH_4NO_3}$  is the binary activity  
236 coefficient for  $\text{NH}_4\text{NO}_3$  ( $\gamma_{NH_4NO_3} = \gamma_{NH_4} \gamma_{NO_3}$ ), and  $m_{NH_4^+}$  and  $m_{NO_3^-}$  are the molalities of  
237  $\text{NH}_4^+$  and  $\text{NO}_3^-$ , respectively. To calculate  $\gamma_{NH_4NO_3}$  and  $m_{NH_4^+} m_{NO_3^-}$ , the activity  
238 coefficients of the corresponding ions and the aerosol water content were assessed using  
239 the E-AIM (IV) model (<http://www.aim.env.uea.ac.uk/aim/model4/model4a.php>).

240 Combining equations (2) and (3), we obtained the product of the partial pressures of  
241  $\text{NH}_3$  and  $\text{HNO}_3$  ( $P_{HNO_3} P_{NH_3}$ ), obtaining an average of  $\sim 15.2 \pm 26.0 \text{ ppb}^2$  at the MF site.

242 This value was within the range of values (1.0~37.7  $\text{ppb}^2$ ) measured by the IGAC in  
243 the summer of 2017 in Xi'an, a metropolitan city located in the Guanzhong Basin of  
244 inland China that has suffered from serious haze pollution (Wu et al., 2020a). Thus, we

245 believe that  $P_{HNO_3} P_{NH_3}$  variations can be assessed using the above method to a certain  
246 extent. For simplification, the dissociation constant of dry  $\text{NH}_4\text{NO}_3$  particle ( $K_p$ ,  $\text{ppb}^2$ )

247 was thus applied in this study, which can be calculated as a function of temperature  
248 using Eq. 4, as was revealed by Mozurkewich (1993). Despite without considering the  
249 aerosol properties (e.g, acidity, mixing state) that may induce the shift of  $\text{NH}_4\text{NO}_3$   
250 equilibrium states, this assessment method was also applied in the similar work

251 conducted by Lindaas et al. (2021).

252 **3 Results and discussion**

253 **3.1 Overview of PM<sub>2.5</sub> at both sites**

254 **3.1.1 Meteorological conditions and temporal variations in PM<sub>2.5</sub> concentrations**

255 The temporal variations in the 4-hr PM<sub>2.5</sub> mass concentrations, water-soluble ions  
256 and meteorological factors measured at the two sampling sites are illustrated in Figure  
257 2, and the comparisons of the above variables are summarized in Table 1. The average  
258 temperature (T) and relative humidity (RH) at the MF site were 23.2±4.2 °C and  
259 68.9±18.2% (Table 1), respectively, and these values were characterized by marked  
260 diurnal variations, as shown in Figure 2a. However, relatively cold and moist weather  
261 frequently occurred at the MS site, which exhibited less pronounced diurnal T and RH  
262 variations, with variations approximately 8 °C and 6% lower than the mean values  
263 derived at the MF site, respectively. Windy weather (wind speed: 3.2±2.0 m/s) also  
264 prevailed at this sampling site with gusts above 10.0 m/s; this condition is conducive  
265 to the dissipation of pollutants.

266 Overall, the PM<sub>2.5</sub> concentrations measured at the MF site varied from 22.8 µg/m<sup>3</sup> to  
267 245.6 µg/m<sup>3</sup>, with a mean value of 76.0±44.1 µg/m<sup>3</sup>, approximately corresponding to  
268 Grade II (75 µg/m<sup>3</sup>) of the National Ambient Air Quality Standard in China. Even so,  
269 the PM<sub>2.5</sub> levels at Huashan town (i.e., at the MF site) were still higher than those  
270 measured in many typical megacities in the summertime, e.g., Xi'an (37 µg/m<sup>3</sup> in  
271 2017) (Wu et al., 2020b) and Beijing (46.3 µg/m<sup>3</sup> in 2016) (Lv et al., 2019).  
272 Noticeably, stagnant meteorological conditions with increasing RH (> 77%) and

273 relatively low wind speeds (< 2.0 m/s) occurred during the relatively late stage of  
274 observation, leading to a buildup of high PM<sub>2.5</sub> loadings (78.7  $\mu\text{g}/\text{m}^3$  to 245.6  $\mu\text{g}/\text{m}^3$ ).  
275 Such typical haze events last approximately 4 days (12 September to 16 September,  
276 2016), indicating that aerosol pollution is still severe in rural towns despite the notable  
277 air quality improvements recorded in most Chinese urban areas. A similar temporal  
278 PM<sub>2.5</sub> pattern was seen at the MS site, where the average PM<sub>2.5</sub> concentration  
279 (47.0 $\pm$ 38.0  $\mu\text{g}/\text{m}^3$ ) was only 0.62-fold that at the MF site and was within the range of  
280 that measured at the summit of Mt. Tai (37.9  $\mu\text{g}/\text{m}^3$  in 2016) (Yi et al., 2021) and on  
281 Mt. Lushan (55.9  $\mu\text{g}/\text{m}^3$  in 2011) (Li et al., 2015) in summertime. As shown in Figure  
282 2d, a multiday episode (mean PM<sub>2.5</sub>: 106.3  $\mu\text{g}/\text{m}^3$ ) also appeared at the MS site during  
283 the period from 12 September to 15 September, corresponding to the days on which  
284 high surface pollution was recorded. This was indicative of the potential impacts of  
285 surface pollution on air quality in mountainous areas.

286 **3.1.2 Diurnal variation in PM<sub>2.5</sub>**

287 As shown in Figure 2c and 2d, regular diurnal PM<sub>2.5</sub> variations were seen throughout  
288 the whole campaign, especially at the MS site. To reveal the differences in the daily  
289 changes in PM<sub>2.5</sub> between the two sampling sites, the mean diurnal cycles of hourly  
290 PM<sub>2.5</sub> and the boundary layer height (BLH) are depicted in Figure 3. At the MF site, the  
291 PM<sub>2.5</sub> concentration was moderately enhanced during the nighttime, with a daily  
292 maximum (88.2 $\pm$ 53.0  $\mu\text{g}/\text{m}^3$ ) observed at 6:00 local standard time (LST). After sunrise,  
293 PM<sub>2.5</sub> exhibited a decreasing trend until  $\sim$ 15:00 LST, corresponding to thermally driven  
294 boundary-layer growth. Conversely, the aerosol concentrations at the MS site

immediately increased as the boundary layer uplifted in the early morning and peaked at 14:00 LST, when the MS site was located completely within the interior of the boundary layer. Proverbially, anabatic valley winds prevail in mountainous regions during the daytime. Thus, the aerosol-rich air at MF site may be transported aloft by the prevailing valley breeze, leading to significantly enhanced PM<sub>2.5</sub> levels at the MS site in short time periods. This finding was further verified by the similar diurnal NO<sub>2</sub> pattern identified at the MS site, as illustrated in Figure S1. In the forenoon period, continuous enhancement in the NO<sub>2</sub> level was observed at the MS site, with a daily maximum of  $14.4 \pm 53.0 \text{ } \mu\text{g}/\text{m}^3$  (at 11:00 LST); this maximum was ~7-fold the early-morning NO<sub>2</sub> concentration. However, O<sub>3</sub> exhibited indistinctive variations during this period, and this was indicative of less NO<sub>2</sub> being generated from photochemical reactions. As mentioned above, there are no obvious anthropogenic emission sources around the MS site; therefore, our observations indicate the remarkable transport of pollutants from the lower ground surface to higher elevations during the daytime.

Moreover, the PM<sub>2.5</sub> concentrations at the MS site exhibited less nighttime variation, with a modest abatement (Figure 3b). The nocturnal BLH usually remained below the elevation of the MS site; thus, the surface PM<sub>2.5</sub> may have contributed less to the aerosol levels at the MS site at night. To identify the potential spatial sources of nocturnal PM<sub>2.5</sub> at the MS site, a high-elevation CWT analysis was conducted. As illustrated in Figure 4, the CWT values in the daylight hours were mostly concentrated over the sampling site, consistent with our above discussions. However, relatively high nighttime CWT loadings were distributed on Mt. Hua and in its surrounding regions, indicating that

317 regional transport may be a major source of PM<sub>2.5</sub> at the MS site at night. Thus, the  
318 constituents and variations in nocturnal PM<sub>2.5</sub> at the MS site may be mainly the results  
319 of regional features. For verifying the feasibility of vertical transport of air parcel, the  
320 WRF-Chem model was applied here to simulate wind field and the divergence that  
321 represents the expansion-rate of the air mass in unit time. From Figure 5(a), the  
322 southerly winds prevailed at mountain foot area during the whole campaign, which  
323 would blow the pollutants into the valley. And these pollutants at low-elevation can be  
324 transported to the upper layer by the updrafts as indicated by the positive values of  
325 vertical divergence at MF area that decreased with enhanced elevation (Figure 5(b)).  
326 Besides that, we also analyzed the organic compounds in PM<sub>2.5</sub> samples, e.g.,  
327 levoglucosan, BkF and IP+BghiP, which are major tracers for the emissions from  
328 biomass burning, coal combustion and vehicle exhausts, respectively (Wang et al., 2009;  
329 Wu et al., 2020b; Wang et al., 2007). From Figure S2, the indistinctive divergences of  
330 diagnostic ratios and proportion of these organic tracers were found among both  
331 sampling sites, suggesting an insignificant change of the corresponding emission  
332 sources during the transport.

333 **3.2 Characterization of water-soluble ions in PM<sub>2.5</sub>**

334 **3.2.1 Comparisons of water-soluble ions between the two sites**

335 Figure 6 shows the fractional contributions of the chemical compositions to the  
336 PM<sub>2.5</sub> at both sampling sites. As summarized in Table 1, the water-soluble ion level  
337 (WSI, 24.0±15.0  $\mu\text{g}/\text{m}^3$ ) at MF site was comparable to that of organic matter (OM,  
338 OM=1.6×OC) (Wang et al., 2016), with a fractional contribution of ~31% to PM<sub>2.5</sub>

339 (Figure 6). At the MS site, the WSI exhibited lower values ( $19.5\pm16.0\text{ }\mu\text{g}/\text{m}^3$ ), yet the  
340 proportion was moderately enhanced by ~6%. Notably, this elevated contribution of  
341 WSIs was mostly attributed to sulfate and ammonium. Similar patterns in which the  
342 secondary inorganic ions (sulfate, nitrate and ammonium, (SNA)) mass fraction  
343 increased with altitude within the mixing height have also been observed in Terni  
344 Valley (central Italy) (Ferrero et al., 2012) and Salt Lake Valley (US) (Baasandorj et  
345 al., 2017). Among the SNA components, sulfate was the predominant species,  
346 exhibiting slight mass concentration differences between the two sampling sites  
347 ( $10.1\pm6.4\text{ }\mu\text{g}/\text{m}^3$  versus  $9.0\pm7.1\text{ }\mu\text{g}/\text{m}^3$ ). However, an ~4% enhancement in the mass  
348 fraction of sulfate was measured at the MS site. Ammonium also exhibited a similar  
349 feature, accounting for ~5%-7.5% of the  $\text{PM}_{2.5}$ . These sulfate and ammonium mass  
350 concentration homogeneities across the two sites were indicative of the further  
351 formation of these two ions during transport. Unlike sulfate and ammonium, nitrate  
352 and its proportions showed opposite trends, decreasing with elevation; this was  
353 consistent with most of the measured components. Above variation features of SNA  
354 among two sites were found at most of moments in the campaign, except for 12-13  
355 September with a higher SNA concentration at MS site (Figure 2e and 2f). On these  
356 two days MS site remained outside the boundary layers (a.s.l., ~550 m), suggesting  
357 less effect of the surface pollutants on the aerosol upper layers. While, the precursor  
358 masses (~ $12.3\text{ }\mu\text{g}/\text{m}^3$  for  $\text{SO}_2$  and  $8.4\text{ }\mu\text{g}/\text{m}^3$  for  $\text{NO}_2$ ) were insufficient to form so  
359 much SNA at MS site. Thus, the higher SNA aloft on above two days may be mostly  
360 driven by regional or long-range transport. This can be verified by the CWT analysis,

361 of which high loadings were mainly distributed in the west and southwest areas of Mt.  
362 Hua (Figure S3a), and the cities on the air mass transport pathways (e.g., Xi'an and  
363 Weinan) also suffered from moderate haze pollution on these two days (Figure S3b).  
364 On account of the different sources of PM<sub>2.5</sub> between these two days and the  
365 remaining periods, the samples during 12-13 September were excluded in the  
366 followed discussion. Whereas, the residual SNA data still exhibited the similar  
367 variations as mentioned above, and the divergence in nitrate mass concentration and  
368 fractional contribution to PM<sub>2.5</sub> among two sites even became more pronounced  
369 (Figure S4). Moreover, distinct nitrate size distributions were also observed between  
370 the different sites in the summertime of 2020 (Figure S5). From the Figure S5, we can  
371 note that the nitrate at low-elevation was enriched in the fine mode with a minor peak  
372 in the coarse fraction. However, the high-elevation nitrate exhibited a bimodal pattern  
373 with two equivalent peaks in the fine and coarse fractions and was well correlated  
374 with coarse mode calcium but poorly correlated with ammonium ( $R^2=0.51$ ,  $p<0.05$ ).  
375 To our knowledge, ammonium nitrate, a major form of fine-mode particulate nitrate,  
376 can be easily volatilized and converted into gas-phase NH<sub>3</sub> and HNO<sub>3</sub> (Pakkanen,  
377 1996; Harrison and Pio, 1983). Thus, the gaseous HNO<sub>3</sub> volatilized from fine PM  
378 may react with coarse-modal cations (e.g., Ca<sup>2+</sup>, Mg<sup>2+</sup> and Na<sup>+</sup>) to form nonvolatile  
379 salts, leading to that significant nitrate shifts from fine particles to large particles. A  
380 similar phenomenon was also found in our previous study conducted at the summit of  
381 Mt. Hua (Wang et al., 2013). Nonvolatile sulfate was predominantly found in the fine  
382 fraction at both sampling sites, which may support this concept. More evidence for

383 this hypothesis is presented below in section 3.3.

384 The diurnal cycles of the 4-hr sulfate, nitrate and ammonium are illustrated in  
385 Figure S6. As shown in Figure S6, the total SNA concentration at the MF site  
386 exhibited a morning peak from 8:00-12:00 LST; this variation was quite different  
387 from that of PM<sub>2.5</sub>. Such a difference between the total SNA and PM<sub>2.5</sub> at the MF site  
388 could partially be attributed to the lower sampling resolution and enhanced formation  
389 of SNA in the morning. The diurnal total SNA pattern identified at the MS site  
390 coincided with the PM<sub>2.5</sub> pattern, exhibiting a daily maximum reaching  $\sim 21.2 \pm 19.9$   
391  $\mu\text{g}/\text{m}^3$  (from 12:00-16:00 LST), a 1.2-fold increase compared to that measured at the  
392 MF site. Among the SNA components, morning peaks of nitrate and ammonium (from  
393 8:00-12:00 LST) were also observed at the MF site. These nitrate and ammonium at  
394 MF site can contribute to that at the MS site through vertical transport, leading to a  
395 significant enhancement in nitrate and ammonium concentrations aloft with the  
396 afternoon peaks during 12:00-16:00 LST. Even so, the maximum nitrate concentration  
397 at the MS site ( $6.5 \pm 7.4 \mu\text{g}/\text{m}^3$ ) was still lower than that measured at the MF site  
398 ( $8.9 \pm 6.8 \mu\text{g}/\text{m}^3$ ) due to the NH<sub>4</sub>NO<sub>3</sub> volatilization under the transport process, while  
399 ammonium exhibited the opposite trend. This finding was consistent with the above  
400 discussion. Unlike nitrate and ammonium, similar diurnal variations in sulfate were  
401 observed between the two sampling sites, with daily maxima observed from 12:00-  
402 16:00 at both sites. The major sulfate formation pathway during the daytime in  
403 summer is the photooxidation of SO<sub>2</sub> with an OH radical, and the formation rate  
404 facilitated by this process is much lower than that of the nitrate formation process

405 (Seinfeld and Johnh, 2016; Rodhe et al., 1981). Thus, sulfate formation may occur  
406 continuously during vertical transport, leading to smaller difference in the diurnal  
407 cycle of sulfate between the two sites.

408 **3.2.2 Chemical forms of SNA at both sites**

409 As shown in Figure 6, the water-soluble ions considered herein mainly included  
410 sulfate, nitrate and ammonium, which usually exist in the form of ammonium salts  
411 ( $\text{NH}_4\text{HSO}_4$ ,  $(\text{NH}_4)_2\text{SO}_4$ ,  $\text{NH}_4\text{NO}_3$ , and so on). In the  $\text{H}_2\text{SO}_4\text{-HNO}_3\text{-NH}_3$   
412 thermodynamic system,  $\text{H}_2\text{SO}_4$  and  $\text{HNO}_3$  are neutralized by  $\text{NH}_3$  under ammonia-  
413 rich conditions and mainly exist as  $(\text{NH}_4)_2\text{SO}_4$  and  $\text{NH}_4\text{NO}_3$  in aerosols. Conversely,  
414  $\text{H}_2\text{SO}_4$  is converted to  $\text{HSO}_4^-$  in environments with relatively low  $\text{NH}_3$  availabilities.  
415 Thus,  $\text{NH}_4\text{HSO}_4$  and  $\text{NH}_4\text{NO}_3$  may be the dominant aerosol components under such  
416 environmental conditions (Rodhe et al., 1981; Seinfeld and Johnh, 2016). To reveal  
417 the major SNA forms at the different sampling sites considered herein, the theoretical  
418 ammonium concentration was calculated according to thermodynamic equilibrium  
419 with the atmospheric sulfate and nitrate levels. The theoretical ammonium levels were  
420 calculated as follows:

$$\text{NH}_4^+_{\text{theory}} = \left( \frac{[\text{SO}_4^{2-}]}{48} + \frac{[\text{NO}_3^-]}{62} \right) \times 18 \quad (\text{Eq. 5})$$

$$\text{NH}_4^+_{\text{theory}} = \left( \frac{[\text{SO}_4^{2-}]}{96} + \frac{[\text{NO}_3^-]}{62} \right) \times 18 \quad (\text{Eq. 6})$$

421 where  $[\text{SO}_4^{2-}]$  and  $[\text{NO}_3^-]$  represent atmospheric concentrations ( $\mu\text{g}/\text{m}^3$ ). When  
422  $(\text{NH}_4)_2\text{SO}_4$  and  $\text{NH}_4\text{NO}_3$  are the dominant species, the  $\text{NH}_4^+_{\text{theory}}$  can be calculated  
423 using equation (5). In contrast, equation (6) suggests that  $\text{NH}_4\text{HSO}_4$  and  $\text{NH}_4\text{NO}_3$  are  
424 abundantly present in the analyzed aerosols. Figure 7 compares the measured  $\text{NH}_4^+$

425 concentrations with the theoretical  $\text{NH}_4^+$  concentrations derived by the two equations  
426 above. As illustrated in Figure 7(a), the slope of the observational  $\text{NH}_4^+$  values against  
427 the theoretical  $\text{NH}_4^+$  values calculated using equation (6) was much closer to unit at the  
428 MF site than at the MS site, meaning that  $\text{NH}_4\text{HSO}_4$  and  $\text{NH}_4\text{NO}_3$  were the major  
429 chemical forms of SNA at the MF site. However, the opposite pattern was revealed at  
430 the MS site; thus, the upper aerosols were characterized by abundant  $(\text{NH}_4)_2\text{SO}_4$  and  
431  $\text{NH}_4\text{NO}_3$ . We also found that the diurnal variations of the SNA chemical forms in  $\text{PM}_{2.5}$ ,  
432 which we mainly concerned in this study, were insignificant at both sampling sites.  
433 Based on observational data collected during the 2020 summertime, the  $\text{NH}_3$  level at  
434 MF site ( $36.0 \pm 68.0$  ppb) was  $\sim 9$ -fold that at MS site ( $4.1 \pm 2.5$  ppb). Under such  
435 abundant  $\text{NH}_3$  environment, the S(VI) was in the major form of  $\text{NH}_4\text{HSO}_4$  but  
436  $(\text{NH}_4)_2\text{SO}_4$  in relatively low  $\text{NH}_3$  environment, which was somewhat unexpected. As  
437 can be inferred from earlier studies (Seinfeld and Johnh, 2016; Shi et al., 1999), the  
438  $\text{NH}_3$  Henry's law coefficients generally increase in value as the temperature decreases.  
439 Therefore, the lower temperatures measured at the MS site would create a more  
440 favorable environment for ammonia, thus shifting its partitioning toward the particulate  
441 phase. The  $\text{HSO}_4^-$  transported from the MF site would thus be further neutralized to  
442  $\text{SO}_4^{2-}$  by this additional ammonium during transport, leading to the significant  
443 difference observed in the chemical forms of SNA between the two sites. Moreover, as  
444 the chemical component change from  $\text{NH}_4\text{HSO}_4$  to  $(\text{NH}_4)_2\text{SO}_4$ , the aerosol acidity  
445 moderately decreased, showing a higher bulk  $\text{PM}_{2.5}$  pH ( $3.4 \pm 2.2$ ) at relatively clean  
446 upper layer and a lower value ( $2.9 \pm 2.0$ ) at heavily polluted grounds (Table 1). However,

447 the previous studies were generally recognized that the aerosol would become more  
448 acidic when the air parcels were transported from the polluted to cleaner/remote regions  
449 (Liu et al., 1996; Nault et al., 2021). As shown in Table 1, the change in aerosol liquid  
450 water content (ALWC) has an indistinctive difference among both sampling sites (*t*-test,  
451  $p>0.05$ ). Thus, we think that such a reduced aerosol acidity with increasing elevation  
452 in our study was mainly due to the change in chemical component, which was caused  
453 by the different physicochemical behaviors of the semi-volatile species nitrate and  
454 ammonium during transport. More discussions are included in the following section.

### 455 **3.3 Physicochemical behaviors of nitrate and ammonium during transport**

456 According to the above discussion, a conceptual model illustrating the  
457 physicochemical behaviors of nitrate and ammonium during vertical transport was  
458 proposed to explain the chemical composition differences between the two sites. As  
459 shown in Figure 8, surface air parcels containing abundant  $\text{NH}_4\text{HSO}_4$  and  $\text{NH}_4\text{NO}_3$   
460 particles can be transported to the upper atmosphere by the prevailing valley winds,  
461 and during this process, the volatile  $\text{NH}_4\text{NO}_3$  is easily converted to gaseous  $\text{NH}_3$  and  
462  $\text{HNO}_3$ . Subsequently, heterogeneous reactions of the gaseous  $\text{HNO}_3$  with fugitive dust  
463 occur, thus forming nonvolatile salts and resulting in the accumulation of nitrate on  
464 the coarse-mode particles. However, as the temperature decreased, the  $\text{NH}_3$  that  
465 volatilized from the fine particles or was derived from the surface can re-enter the  
466 particulate phase through the gas–particle partition. Therefore,  $(\text{NH}_4)_2\text{SO}_4$  would be  
467 formed in the aerosol phase and would gradually replace  $\text{NH}_4\text{HSO}_4$ .

468 To investigate the likelihood of  $\text{NH}_4\text{NO}_3$  volatilization during the transport process,

469 the dissociation constant of  $\text{NH}_4\text{NO}_3$  ( $K_p$ ) and the partial pressures of gas-phase  $\text{NH}_3$   
470 and  $\text{HNO}_3$  were calculated in this study. More details regarding the calculation steps  
471 of the above factors can be found in section 2.4. Based on the thermodynamic  
472 principles presented by Stelson and Seinfeld (1982), when the product of the partial  
473 pressures of  $\text{NH}_3$  and  $\text{HNO}_3$  ( $P_{\text{HNO}_3} \times P_{\text{NH}_3}$ ) is greater than  $K_p$ , the equilibrium of the  
474 system shifts toward the aerosol phase, thus increasing  $\text{NH}_4\text{NO}_3$  formation. In  
475 contrast, a relatively low  $P_{\text{HNO}_3} \times P_{\text{NH}_3}/K_p$  value (<1) suggests that  $\text{NH}_4\text{NO}_3$   
476 dissociation is induced and that  $\text{NH}_4\text{NO}_3$  is transferred to the gas phase. Figure 9  
477 depicts the ratio of the product of the partial pressures of  $\text{NH}_3$  and  $\text{HNO}_3$  with  
478 different ambient temperatures. As shown in Figure 9, approximately 85% of the  
479 samples collected at both sampling sites were located within the region with  
480  $P_{\text{HNO}_3} \times P_{\text{NH}_3}/K_p$  less than 1, demonstrating a common  $\text{NH}_4\text{NO}_3$  dissociation  
481 phenomenon during the observed period. For the samples with  $P_{\text{HNO}_3} \times P_{\text{NH}_3}/K_p$  ratios  
482 <1, the mean value of the MS-site ratios was approximately half that of the MF-site  
483 ratios, indicating that  $\text{NH}_4\text{NO}_3$  dissociation may be more likely at higher elevations  
484 than that at lower elevations. This finding was inconsistent with the aircraft  
485 observations of the wildfire smoke plumes collected by Lindaas et al. (2021), who  
486 revealed that  $P_{\text{HNO}_3} \times P_{\text{NH}_3}/K_p$  exhibited an increasing trend within 1-3 km (a.s.l.). As  
487 we know, the abundant  $\text{NH}_3$  and  $\text{NO}_x$  can be emitted by the wildfire, which would be  
488 transported aloft and lead to a higher  $\text{NH}_3$  and  $\text{HNO}_3$  mixing ratio compared to that at  
489 lower elevation. This may drive a higher  $P_{\text{HNO}_3} \times P_{\text{NH}_3}/K_p$  ratio at the upper layers of  
490 aircraft observations in the western U.S. (Lindaas et al., 2021).

Moreover, the nitrogen isotope compositions of nitrate and ammonium in PM<sub>2.5</sub> that can retain invaluable information regarding physicochemical processes (Wiedenhaus et al., 2021; Elliott et al., 2019), were thus measured to further verify the conceptual model. As previously mentioned, unlike daytime pollutants, nocturnal pollutants exhibited different sources between the two sampling sites. Thus, their nitrogen isotope compositions were more complicated and less comparable. However, for simplicity, only the daytime samples were analyzed herein based on the hypothesis that the sources of the high-elevation pollutants were the same as those of the pollutants collected at the MF site. As shown in Figure 10, a discrepancy in the  $\delta^{15}\text{N}$  value of nitrate ( $\delta^{15}\text{N-NO}_3^-$ ) featuring more <sup>15</sup>N-enriched  $\text{NO}_3^-$  was observed at the MS site, with a *p* value less than 0.05. This finding can be ascribed to the evaporation of a portion of the particulate  $\text{NH}_4\text{NO}_3$  due to a dissociation shift in equilibrium; in this shift, the lighter <sup>14</sup>N was preferentially incorporated into the atmosphere, leading to <sup>15</sup>N enrichment in the remaining nitrate. Similar phenomenon was also revealed by Wiedenhaus et al. (2021), who thought that the ammonium nitrate dissociation may be an important reason for the accumulation of <sup>15</sup>N in aerosol particles. Additionally, Freyer et al. (1993) revealed that gas-phase isotopic exchanges between NO and  $\text{NO}_2$  result in the enrichment of the heavier <sup>15</sup>N isotope in the more oxidized form and may further affect  $\delta^{15}\text{N-NO}_3^-$  through nitrate formation reactions. The above isotopic exchange between  $\text{NO}_2$  and  $\text{NO}_x$  can be roughly described as follows:  $[\delta^{15}\text{N}(\text{NO}_2) - \delta^{15}\text{N}(\text{NO}_x)] = (1 - K) \times (1 - f_{\text{NO}_2})$ , where *K* and *f<sub>NO</sub>2* are the temperature-dependent exchange constant and mole fraction of  $\text{NO}_2$ , respectively. Based on trace gas

513 observations, the  $f_{\text{NO}_2}$  values of the air aloft were very high due to the frequently  
514 undetectable NO concentration, indicating a rather limited isotopic exchange between  
515  $\text{NO}_2$  and NO. Therefore, the evaporation of particulate  $\text{NH}_4\text{NO}_3$  have been the  
516 significant factor affecting the measurement of a higher  $\delta^{15}\text{N-NO}_3^-$  at the MS site than  
517 at the MF site in our observations. According to the above analysis, the ammonium at  
518 MS site should theoretically be more and more enriched in  $\delta^{15}\text{N}$  with the continuous  
519  $\text{NH}_4\text{NO}_3$  volatilization. However, our observation of  $\delta^{15}\text{N-NH}_4^+$  did not correspond to  
520 above pattern, namely, ammonium at the MS site depleted in  $\delta^{15}\text{N}$  compared to that at  
521 MF site ( $p < 0.05$ , Figure 10). Given the unchanged  $\text{NH}_3$  sources as verified in section  
522 3.1.2, such seemingly unreasonable observations were mainly caused by the gas-to-  
523 particle conversion of ammonia. In this process, the reversible phase-equilibrium  
524 reactions between  $\text{NH}_3(\text{g})$  and  $\text{HNO}_3(\text{g})/\text{HCl}(\text{g})$  would yield positive enrichment in  
525  $\delta^{15}\text{N}$  of aerosol  $\text{NH}_4^+$  (Walters et al., 2019); nevertheless, unidirectional reactions  
526 involving  $\text{NH}_3(\text{g})$  and  $\text{SO}_4^{2-}/\text{HSO}_4^-$  favored  $^{15}\text{N}$  depletion in the particle form as  
527 revealed by Heaton et al. (1997). Thereby, the lower  $\delta^{15}\text{N-NH}_4^+$  values at MS site  
528 were mostly driven by those irreversible reactions, rather than the reversible  
529 equilibrium ones. This result further confirmed our conjecture that the additional  $\text{NH}_3$   
530 would partition into particulate phases and further neutralize the acidic  $\text{NH}_4\text{HSO}_4$ ,  
531 leading to an increasing pH at MS site compared to that at MF site. Taken together,  
532 this compelling evidence verifies that fine-mode nitrate and ammonium exhibit  
533 distinctly different physicochemical behaviors during their transport.

534 **4 Conclusions and atmospheric implications**

535 In this study, aerosol samples were collected at 4-hr intervals on the mountainside  
536 of Mt. Hua, and the OC, EC, water-soluble ions and isotope compositions of nitrate  
537 and ammonium were measured and compared with simultaneous observations taken  
538 at a lower-elevation site (MF site). The particle mass at the MF site was  
539 approximately 1.5-fold that at the MS site, and distinctly different diurnal cycles were  
540 observed between the two sampling sites. Based on the BLH variation, we revealed  
541 that near-surface PM<sub>2.5</sub> could be transported to the upper layers by the mountain-  
542 valley breeze, leading to the gradual accumulation of pollutants on the mountainside  
543 during the daytime.

544 Sulfate, the predominant species found among ions at both sampling sites,  
545 exhibited nearly identical mass concentrations at the two sites but had a moderately  
546 enhanced mass fraction at MS site. Such homogeneity was also observed in  
547 ammonium, which mainly existed as NH<sub>4</sub>HSO<sub>4</sub>+NH<sub>4</sub>NO<sub>3</sub> and (NH<sub>4</sub>)<sub>2</sub>SO<sub>4</sub>+NH<sub>4</sub>NO<sub>3</sub> at  
548 the MF and MS sites, respectively. This observation indicated the further formation of  
549 ammonium during the transport process. Unlike sulfate and ammonium, nitrate at the  
550 MS site exhibited abated trends in both its concentration and proportion, mainly due  
551 to the volatilization of NH<sub>4</sub>NO<sub>3</sub>. With the help of nitrate and ammonium nitrogen  
552 isotopes, we proposed a conceptual model to illustrate the different behaviors of  
553 nitrate and ammonium during vertical transport; in this model, the semivolatile  
554 NH<sub>4</sub>NO<sub>3</sub> in surface air parcels was easily converted into gaseous NH<sub>3</sub> and HNO<sub>3</sub>.  
555 Subsequently, heterogeneous reactions occurred between this gaseous HNO<sub>3</sub> and  
556 fugitive dust, forming nonvolatile salts and leading to a significant nitrate shift from

557 fine particles into coarse particles. In addition, the decreasing temperature was  
558 favorable for NH<sub>3</sub> partitioning toward the particle phase, and the addition of  
559 ammonium further neutralized HSO<sub>4</sub><sup>-</sup> to form SO<sub>4</sub><sup>2-</sup>. This process would reduce the  
560 aerosol acidity, with bulk PM<sub>2.5</sub> pH increasing from 2.9±2.0 at MF site to 3.4±2.2 at  
561 MS site.

562 Over the past decade, the relative abundance of NH<sub>4</sub>NO<sub>3</sub> has been enhanced in  
563 most urban areas of China because strict emission directives have been promulgated  
564 to abate the emission and environmental impacts of SO<sub>2</sub> (Xie et al., 2020; Song et al.,  
565 2019). In this work, we observed that NH<sub>4</sub>NO<sub>3</sub> volatilization was a ubiquitous  
566 phenomenon for particles during transport, resulting in a shift in partwise nitrate from  
567 the fine mode to the coarse fraction; this shift has also been reported in the offshore  
568 areas of the UK (Yeatman et al., 2001). Thus, we think that considering only fine-  
569 fraction nitrate may result in the conversion rate of NO<sub>x</sub> to nitrate being partly  
570 underestimated at some times, especially in the summer. Moreover, the deposition  
571 velocity of coarse particles is usually faster than that of fine particles; therefore, the  
572 above process would appreciably elevate the deposition of N into the environment.  
573 Indeed, abundant NO<sub>2</sub>, O<sub>3</sub> and NH<sub>3</sub> co-occurrence is common in the East Asian  
574 atmosphere, and under these conditions, secondary inorganic aerosols can be  
575 effectively produced, leading to a PM<sub>2.5</sub> loading explosion in the urban atmosphere of  
576 China (Wu et al., 2020c; Wang et al., 2016). Given this, harmonious reductions in  
577 NO<sub>2</sub>, O<sub>3</sub> and NH<sub>3</sub> will be urgent in further mitigation strategies to improve air quality  
578 and alleviate other potential effects.

579

580 **Author contributions.** GW designed the experiment. CW, JiaL and CC collected the  
581 samples. CW and CC conducted the experiments. CW and GW performed the data  
582 interpretation and wrote the paper. All authors contributed to the paper with useful  
583 scientific discussions or comments.

584

585 **Competing interests.** The authors declare that they have no conflict of interest.

586

587 **Acknowledgements.** This work was financially supported by the National Natural  
588 Science Foundation of China (No. 42130704, 42007202), Shanghai Science and  
589 Technology Innovation Action Plan (20dz1204000) and ECNU Happiness Flower  
590 program. We thank Lang Liu from School of Public Policy and Administration,  
591 Northwestern Polytechnical University, Xi'an, China for his support of model  
592 simulation in meteorological data during the campaign.

593

594

595

## 596 **References**

597 Andreae, M. O. and Ramanathan, V.: Climate's Dark Forcings, *Science*, 340, 280-281,  
598 10.1126/science.1235731, 2013.

599 Baasandorj, M., Hoch, S. W., Bares, R., Lin, J. C., Brown, S. S., Millet, D. B., Martin, R., Kelly, K.,  
600 Zarzana, K. J., Whiteman, C. D., Dube, W. P., Tonnesen, G., Jaramillo, I. C., and Sohl, J.: Coupling  
601 between Chemical and Meteorological Processes under Persistent Cold-Air Pool Conditions:  
602 Evolution of Wintertime PM2.5 Pollution Events and N2O5 Observations in Utah's Salt Lake Valley,  
603 *Environ. Sci. Technol.*, 51, 5941-5950, 10.1021/acs.est.6b06603, 2017.

604 Bond, T. C., Doherty, S. J., Fahey, D. W., Forster, P. M., Berntsen, T., DeAngelo, B. J., Flanner, M. G.,  
605 Ghan, S., Kaercher, B., Koch, D., Kinne, S., Kondo, Y., Quinn, P. K., Sarofim, M. C., Schultz, M.  
606 G., Schulz, M., Venkataraman, C., Zhang, H., Zhang, S., Bellouin, N., Guttikunda, S. K., Hopke, P.  
607 K., Jacobson, M. Z., Kaiser, J. W., Klimont, Z., Lohmann, U., Schwarz, J. P., Shindell, D., Storelvmo,  
608 T., Warren, S. G., and Zender, C. S.: Bounding the role of black carbon in the climate system: A

609 scientific assessment, *J. Geophys. Res.-Atmos.*, 118, 5380-5552, 10.1002/jgrd.50171, 2013.

610 Carslaw, K. S., Lee, L. A., Reddington, C. L., Pringle, K. J., Rap, A., Forster, P. M., Mann, G. W.,  
611 Spracklen, D. V., Woodhouse, M. T., Regayre, L. A., and Pierce, J. R.: Large contribution of natural  
612 aerosols to uncertainty in indirect forcing, *Nat.*, 503, 67-+, 10.1038/nature12674, 2013.

613 Dzepina, K., Mazzoleni, C., Fialho, P., China, S., Zhang, B., Owen, R. C., Helmig, D., Hueber, J., Kumar,  
614 S., Perlinger, J. A., Kramer, L. J., Dziobak, M. P., Ampadu, M. T., Olsen, S., Wuebbles, D. J., and  
615 Mazzoleni, L. R.: Molecular characterization of free tropospheric aerosol collected at the Pico  
616 Mountain Observatory: a case study with a long-range transported biomass burning plume, *Atmos.*  
617 *Chem. Phys.*, 15, 5047-5068, 10.5194/acp-15-5047-2015, 2015.

618 Elliott, E. M., Yu, Z., Cole, A. S., and Coughlin, J. G.: Isotopic advances in understanding reactive  
619 nitrogen deposition and atmospheric processing, *Sci. Total Environ.*, 662, 393-403,  
620 10.1016/j.scitotenv.2018.12.177, 2019.

621 Fan, J., Rosenfeld, D., Zhang, Y., Giangrande, S. E., Li, Z., Machado, L. A. T., Martin, S. T., Yang, Y.,  
622 Wang, J., Artaxo, P., Barbosa, H. M. J., Braga, R. C., Comstock, J. M., Feng, Z., Gao, W., Gomes,  
623 H. B., Mei, F., Poehlker, C., Poehlker, M. L., Poeschl, U., and de Souza, R. A. F.: Substantial  
624 convection and precipitation enhancements by ultrafine aerosol particles, *Science*, 359, 411-+,  
625 10.1126/science.aan8461, 2018.

626 Fan, M.-Y., Zhang, Y.-L., Lin, Y.-C., Hong, Y., Zhao, Z.-Y., Xie, F., Du, W., Cao, F., Sun, Y., and Fu, P.:  
627 Important Role of NO<sub>3</sub> Radical to Nitrate Formation Aloft in Urban Beijing: Insights from Triple  
628 Oxygen Isotopes Measured at the Tower, *Environ. Sci. Technol.*, 10.1021/acs.est.1c02843, 2021.

629 Fang, Y. T., Koba, K., Wang, X. M., Wen, D. Z., Li, J., Takebayashi, Y., Liu, X. Y., and Yoh, M.:  
630 Anthropogenic imprints on nitrogen and oxygen isotopic composition of precipitation nitrate in a  
631 nitrogen-polluted city in southern China, *Atmos. Chem. Phys.*, 11, 1313-1325, 10.5194/acp-11-  
632 1313-2011, 2011.

633 Ferrero, L., Cappelletti, D., Moroni, B., Sangiorgi, G., Perrone, M. G., Crocchianti, S., and Bolzacchini,  
634 E.: Wintertime aerosol dynamics and chemical composition across the mixing layer over basin  
635 valleys, *Atmos. Environ.*, 56, 143-153, 10.1016/j.atmosenv.2012.03.071, 2012.

636 Freyer, H. D., Kley, D., Volz-Thomas, A., and Kobel, K.: On the interaction of isotopic exchange  
637 processes with photochemical reactions in atmospheric oxides of nitrogen, *Journal of Geophysical  
638 Research*, 98, 14791-14796, 10.1029/93jd00874, 1993.

639 Fuzzi, S., Baltensperger, U., Carslaw, K., Decesari, S., van der Gon, H. D., Facchini, M. C., Fowler, D.,  
640 Koren, I., Langford, B., Lohmann, U., Nemitz, E., Pandis, S., Riipinen, I., Rudich, Y., Schaap, M.,  
641 Slowik, J. G., Spracklen, D. V., Vignati, E., Wild, M., Williams, M., and Gilardoni, S.: Particulate  
642 matter, air quality and climate: lessons learned and future needs, *Atmos. Chem. Phys.*, 15, 8217-  
643 8299, 10.5194/acp-15-8217-2015, 2015.

644 Guo, S., Hu, M., Zamora, M. L., Peng, J., Shang, D., Zheng, J., Du, Z., Wu, Z., Shao, M., Zeng, L.,  
645 Molina, M. J., and Zhang, R.: Elucidating severe urban haze formation in China, *Proc. Natl. Acad.  
646 Sci. USA*, 111, 17373-17378, 10.1073/pnas.1419604111, 2014.

647 Harrison, R. M. and Pio, C. A.: Size-differentiated composition of inorganic atmospheric aerosols of both  
648 marine and polluted continental origin, *Atmos. Environ.*, 17, 1733-1738, 10.1016/0004-  
649 6981(83)90180-4, 1983.

650 Heaton, T. H. E., Spiro, B., Madeline, S., and Robertson, C.: Potential canopy influences on the isotopic  
651 composition of nitrogen and sulphur in atmospheric deposition, *Oecologia*, 109, 600-607,  
652 10.1007/s004420050122, 1997.

653 Lambey, V. and Prasad, A. D.: A Review on Air Quality Measurement Using an Unmanned Aerial Vehicle,  
654 Water, Air, & Soil Pollution, 232, 10.1007/s11270-020-04973-5, 2021.

655 Lelieveld, J., Evans, J. S., Fnais, M., Giannadaki, D., and Pozzer, A.: The contribution of outdoor air  
656 pollution sources to premature mortality on a global scale, Nat., 525, 367-+, 10.1038/nature15371,  
657 2015.

658 Li, D., Wu, C., Zhang, S., Lei, Y., Lv, S., Du, W., Liu, S., Zhang, F., Liu, X., Liu, L., Meng, J., Wang, Y.,  
659 Gao, J., and Wang, G.: Significant coal combustion contribution to water-soluble brown carbon  
660 during winter in Xingtai, China: Optical properties and sources, J. Environ. Sci., 124, 892-900,  
661 10.1016/j.jes.2022.02.026, 2023.

662 Li, J. J., Wang, G. H., Cao, J. J., Wang, X. M., and Zhang, R. J.: Observation of biogenic secondary  
663 organic aerosols in the atmosphere of a mountain site in central China: temperature and relative  
664 humidity effects, Atmos. Chem. Phys., 13, 11535-11549, 10.5194/acp-13-11535-2013, 2013.

665 Li, T., Wang, Y., Li, W. J., Chen, J. M., Wang, T., and Wang, W. X.: Concentrations and solubility of trace  
666 elements in fine particles at a mountain site, southern China: regional sources and cloud processing,  
667 Atmos. Chem. Phys., 15, 8987-9002, 10.5194/acp-15-8987-2015, 2015.

668 Li, W., Shao, L., Zhang, D., Ro, C.-U., Hu, M., Bi, X., Geng, H., Matsuki, A., Niu, H., and Chen, J.: A  
669 review of single aerosol particle studies in the atmosphere of East Asia: morphology, mixing state,  
670 source, and heterogeneous reactions, Journal of Cleaner Production, 112, 1330-1349,  
671 10.1016/j.jclepro.2015.04.050, 2016.

672 Lindaas, J., Pollack, I. B., Calahorrano, J. J., O'Dell, K., Garofalo, L. A., Pothier, M. A., Farmer, D. K.,  
673 Kreidenweis, S. M., Campos, T., Flocke, F., Weinheimer, A. J., Montzka, D. D., Tyndall, G. S., Apel,  
674 E. C., Hills, A. J., Hornbrook, R. S., Palm, B. B., Peng, Q., Thornton, J. A., Permar, W., Wielgasz,  
675 C., Hu, L., Pierce, J. R., Collett, J. L., Jr., Sullivan, A. P., and Fischer, E. V.: Empirical Insights Into  
676 the Fate of Ammonia in Western US Wildfire Smoke Plumes, J. Geophys. Res.-Atmos., 126,  
677 10.1029/2020jd033730, 2021.

678 Liu, D., Fang, Y., Tu, Y., and Pan, Y.: Chemical Method for Nitrogen Isotopic Analysis of Ammonium at  
679 Natural Abundance, Anal. Chem., 86, 3787-3792, 10.1021/ac403756u, 2014.

680 Liu, L. J. S., Burton, R., Wilson, W. E., and Koutrakis, P.: Comparison of aerosol acidity in urban and  
681 semirural environments, Atmos. Environ., 30, 1237-1245, 10.1016/1352-2310(95)00438-6, 1996.

682 Liu, T., Chan, A. W. H., and Abbatt, J. P. D.: Multiphase Oxidation of Sulfur Dioxide in Aerosol Particles:  
683 Implications for Sulfate Formation in Polluted Environments, Environ. Sci. Technol., 55, 4227-4242,  
684 10.1021/acs.est.0c06496, 2021.

685 Lv, D., Chen, Y., Zhu, T., Li, T., Shen, F., Li, X., and Mehmood, T.: The pollution characteristics of PM10  
686 and PM2.5 during summer and winter in Beijing, Suning and Islamabad, Atmospheric Pollution  
687 Research, 10, 1159-1164, 10.1016/j.apr.2019.01.021, 2019.

688 Lv, S., Wang, F., Wu, C., Chen, Y., Liu, S., Zhang, S., Li, D., Du, W., Zhang, F., Wang, H., Huang, C.,  
689 Fu, Q., Duan, Y., and Wang, G.: Gas-to-Aerosol Phase Partitioning of Atmospheric Water-Soluble  
690 Organic Compounds at a Rural Site in China: An Enhancing Effect of NH<sub>3</sub> on SOA Formation,  
691 Environ. Sci. Technol., 56, 3915-3924, 10.1021/acs.est.1c06855, 2022.

692 Meng, J., Wang, G., Hou, Z., Liu, X., Wei, B., Wu, C., Cao, C., Wang, J., Li, J., Cao, J., Zhang, E., Dong,  
693 J., Liu, J., Ge, S., and Xie, Y.: Molecular distribution and stable carbon isotopic compositions of  
694 dicarboxylic acids and related SOA from biogenic sources in the summertime atmosphere of Mt.  
695 Tai in the North China Plain, Atmos. Chem. Phys., 18, 15069-15086, 10.5194/acp-18-15069-2018,  
696 2018.

697 Mozurkewich, M.: The dissociation constant of ammonium nitrate and its dependence on temperature,  
698 relative humidity and particle size, *Atmospheric Environment. Part A. General Topics*, 27, 261-270,  
699 1993.

700 Nault, B. A., Campuzano-Jost, P., Day, D. A., Jo, D. S., Schroder, J. C., Allen, H. M., Bahreini, R., Bian,  
701 H., Blake, D. R., Chin, M., Clegg, S. L., Colarco, P. R., Crounse, J. D., Cubison, M. J., DeCarlo, P.  
702 F., Dibb, J. E., Diskin, G. S., Hodzic, A., Hu, W., Katich, J. M., Kim, M. J., Kodros, J. K., Kupec, A.,  
703 Lopez-Hilfiker, F. D., Marais, E. A., Middlebrook, A. M., Andrew Neuman, J., Nowak, J. B., Palm,  
704 B. B., Paulot, F., Pierce, J. R., Schill, G. P., Scheuer, E., Thornton, J. A., Tsigaridis, K., Wennberg,  
705 P. O., Williamson, C. J., and Jimenez, J. L.: Chemical transport models often underestimate  
706 inorganic aerosol acidity in remote regions of the atmosphere, *Communications Earth &*  
707 *Environment*, 2, 10.1038/s43247-021-00164-0, 2021.

708 Pakkanen, T. A.: Study of formation of coarse particle nitrate aerosol, *Atmos. Environ.*, 30, 2475-2482,  
709 10.1016/1352-2310(95)00492-0, 1996.

710 Petit, J. E., Favez, O., Albinet, A., and Canonaco, F.: A user-friendly tool for comprehensive evaluation  
711 of the geographical origins of atmospheric pollution: Wind and trajectory analyses, *Environmental*  
712 *Modelling & Software*, 88, 183-187, 10.1016/j.envsoft.2016.11.022, 2017.

713 Raes, F., Van Dingenen, R., Vignati, E., Wilson, J., Putaud, J. P., Seinfeld, J. H., and Adams, P.: Formation  
714 and cycling of aerosols in the global troposphere, *Atmos. Environ.*, 34, 4215-4240, 10.1016/s1352-  
715 2310(00)00239-9, 2000.

716 Reid, J. S., Kuehn, R. E., Holz, R. E., Eloranta, E. W., Kaku, K. C., Kuang, S., Newchurch, M. J.,  
717 Thompson, A. M., Trepte, C. R., Zhang, J., Atwood, S. A., Hand, J. L., Holben, B. N., Minnis, P.,  
718 and Posselt, D. J.: Ground-based High Spectral Resolution Lidar observation of aerosol vertical  
719 distribution in the summertime Southeast United States, *J. Geophys. Res.-Atmos.*, 122, 2970-3004,  
720 10.1002/2016jd025798, 2017.

721 rganization, W. H.: WHO global air quality guidelines: particulate matter (PM2. 5 and PM10), ozone,  
722 nitrogen dioxide, sulfur dioxide and carbon monoxide, World Health Organization2021.

723 Rodhe, H., Crutzen, P., and Vanderpol, A.: Formation of sulfuric and nitric acid in the atmosphere during  
724 long-range transport, *Tellus*, 33, 132-141, 1981.

725 Seinfeld and JohnH: *Atmospheric chemistry and physics : from air pollution to climate change / 3nd ed.*,  
726 *Atmospheric chemistry and physics : from air pollution to climate change / 3nd ed*2016.

727 Shi, Q., Davidovits, P., Jayne, J. T., Worsnop, D. R., and Kolb, C. E.: Uptake of gas-phase ammonia. 1.  
728 Uptake by aqueous surfaces as a function of pH, *J. Phys. Chem. A*, 103, 8812-8823,  
729 10.1021/jp991696p, 1999.

730 Shiraiwa, M., Ueda, K., Pozzer, A., Lammel, G., Kampf, C. J., Fushimi, A., Enami, S., Arangio, A. M.,  
731 Froehlich-Nowoisky, J., Fujitani, Y., Furuyama, A., Lakey, P. S. J., Lelieveld, J., Lucas, K., Morino,  
732 Y., Poeschl, U., Takahama, S., Takami, A., Tong, H., Weber, B., Yoshino, A., and Sato, K.: Aerosol  
733 Health Effects from Molecular to Global Scales, *Environ. Sci. Technol.*, 51, 13545-13567,  
734 10.1021/acs.est.7b04417, 2017.

735 Song, S., Nenes, A., Gao, M., Zhang, Y., Liu, P., Shao, J., Ye, D., Xu, W., Lei, L., Sun, Y., Liu, B., Wang,  
736 S., and McElroy, M. B.: Thermodynamic Modeling Suggests Declines in Water Uptake and Acidity  
737 of Inorganic Aerosols in Beijing Winter Haze Events during 2014/2015-2018/2019, *Environmental*  
738 *Science & Technology Letters*, 6, 752-760, 10.1021/acs.estlett.9b00621, 2019.

739 Stelson, A. W. and Seinfeld, J. H.: Relative humidity and temperature dependence of the ammonium  
740 nitrate dissociation constant, *Atmos. Environ.*, 16, 983-992, 10.1016/0004-6981(82)90184-6, 1982.

741 Tang, I. N. and Munkelwitz, H. R.: Composition and temperature dependence of the deliquescence  
742 properties of hygroscopic aerosols, *Atmos. Environ.*, 27, 467-473, 1993.

743 van Donkelaar, A., Martin, R. V., Brauer, M., Hsu, N. C., Kahn, R. A., Levy, R. C., Lyapustin, A., Sayer,  
744 A. M., and Winker, D. M.: Global Estimates of Fine Particulate Matter using a Combined  
745 Geophysical-Statistical Method with Information from Satellites, Models, and Monitors, *Environ.*  
746 *Sci. Technol.*, 50, 3762-3772, 10.1021/acs.est.5b05833, 2016.

747 Walters, W. W., Chai, J., and Hastings, M. G.: Theoretical Phase Resolved Ammonia-Ammonium  
748 Nitrogen Equilibrium Isotope Exchange Fractionations: Applications for Tracking Atmospheric  
749 Ammonia Gas-to-Particle Conversion, *ACS Earth Space Chem.*, 3, 79-89,  
750 10.1021/acsearthspacechem.8b00140, 2019.

751 Wang, G., Kawamura, K., Hatakeyama, S., Takami, A., Li, H., and Wang, W.: Aircraft measurement of  
752 organic aerosols over China, *Environ. Sci. Technol.*, 41, 3115-3120, 10.1021/es062601h, 2007.

753 Wang, G., Kawamura, K., Xie, M., Hu, S., Gao, S., Cao, J., An, Z., and Wang, Z.: Size-distributions of  
754 n-alkanes, PAHs and hopanes and their sources in the urban, mountain and marine atmospheres over  
755 East Asia, *Atmos. Chem. Phys.*, 9, 8869-8882, 10.5194/acp-9-8869-2009, 2009.

756 Wang, G., Kawamura, K., Xie, M., Hu, S., Li, J., Zhou, B., Cao, J., and An, Z.: Selected water-soluble  
757 organic compounds found in size-resolved aerosols collected from urban, mountain and marine  
758 atmospheres over East Asia, *Tellus Series B-Chemical and Physical Meteorology*, 63, 371-381,  
759 10.1111/j.1600-0889.2011.00536.x, 2011.

760 Wang, G., Zhang, R., Gomez, M. E., Yang, L., Zamora, M. L., Hu, M., Lin, Y., Peng, J., Guo, S., Meng,  
761 J., Li, J., Cheng, C., Hu, T., Ren, Y., Wang, Y., Gao, J., Cao, J., An, Z., Zhou, W., Li, G., Wang, J.,  
762 Tian, P., Marrero-Ortiz, W., Secretst, J., Du, Z., Zheng, J., Shang, D., Zeng, L., Shao, M., Wang, W.,  
763 Huang, Y., Wang, Y., Zhu, Y., Li, Y., Hu, J., Pan, B., Cai, L., Cheng, Y., Ji, Y., Zhang, F., Rosenfeld,  
764 D., Liss, P. S., Duce, R. A., Kolb, C. E., and Molina, M. J.: Persistent sulfate formation from London  
765 Fog to Chinese haze, *Proc. Natl. Acad. Sci. USA*, 113, 13630-13635, 10.1073/pnas.1616540113,  
766 2016.

767 Wang, G. H., Zhou, B. H., Cheng, C. L., Cao, J. J., Li, J. J., Meng, J. J., Tao, J., Zhang, R. J., and Fu, P.  
768 Q.: Impact of Gobi desert dust on aerosol chemistry of Xi'an, inland China during spring 2009:  
769 differences in composition and size distribution between the urban ground surface and the mountain  
770 atmosphere, *Atmos. Chem. Phys.*, 13, 819-835, 10.5194/acp-13-819-2013, 2013.

771 Wankel, S. D., Chen, Y., Kendall, C., Post, A. F., and Paytan, A.: Sources of aerosol nitrate to the Gulf of  
772 Aqaba: Evidence from delta N-15 and delta O-18 of nitrate and trace metal chemistry, *Mar. Chem.*,  
773 120, 90-99, 10.1016/j.marchem.2009.01.013, 2010.

774 Wexler, A. S. and Seinfeld, J. H.: Second-generation inorganic aerosol model, *Atmos. Environ.*, 25A,  
775 2731-2748, 1991.

776 Wiedenhaus, H., Ehrnsperger, L., Klemm, O., and Strauss, H.: Stable N-15 isotopes in fine and coarse  
777 urban particulate matter, *Aerosol Sci. Technol.*, 55, 859-870, 10.1080/02786826.2021.1905150,  
778 2021.

779 Wu, C., Liu, L., Wang, G., Zhang, S., Li, G., Lv, S., Li, J., Wang, F., Meng, J., and Zeng, Y.: Important  
780 contribution of N2O5 hydrolysis to the daytime nitrate in Xi'an, China during haze periods: Isotopic  
781 analysis and WRF-Chem model simulation, *Environmental pollution (Barking, Essex : 1987)*, 288,  
782 117712-117712, 10.1016/j.envpol.2021.117712, 2021.

783 Wu, C., Wang, G., Li, J., Li, J., Cao, C., Ge, S., Xie, Y., Chen, J., Liu, S., Du, W., Zhao, Z., and Cao, F.:  
784 Non-agricultural sources dominate the atmospheric NH3 in Xi'an, a megacity in the semi-arid region

785 of China, *Sci. Total Environ.*, 722, 137756, 10.1016/j.scitotenv.2020.137756, 2020a.

786 Wu, C., Wang, G., Li, J., Li, J., Cao, C., Ge, S., Xie, Y., Chen, J., Li, X., Xue, G., Wang, X., Zhao, Z.,  
787 and Cao, F.: The characteristics of atmospheric brown carbon in Xi'an, inland China: sources, size  
788 distributions and optical properties, *Atmos. Chem. Phys.*, 20, 2017-2030, 10.5194/acp-20-2017-  
789 2020, 2020b.

790 Wu, C., Zhang, S., Wang, G., Lv, S., Li, D., Liu, L., Li, J., Liu, S., Du, W., Meng, J., Qiao, L., Zhou, M.,  
791 Huang, C., and Wang, H.: Efficient Heterogeneous Formation of Ammonium Nitrate on the Saline  
792 Mineral Particle Surface in the Atmosphere of East Asia during Dust Storm Periods, *Environ. Sci.*  
793 *Technol.*, 54, 15622-15630, 10.1021/acs.est.0c04544, 2020c.

794 Xie, Y., Wang, G., Wang, X., Chen, J., Chen, Y., Tang, G., Wang, L., Ge, S., Xue, G., Wang, Y., and Gao,  
795 J.: Nitrate-dominated PM<sub>2.5</sub> and elevation of particle pH observed in urban Beijing during the  
796 winter of 2017, *Atmos. Chem. Phys.*, 20, 5019-5033, 10.5194/acp-20-5019-2020, 2020.

797 Xu, Z., Huang, X., Nie, W., Shen, Y., Zheng, L., Xie, Y., Wang, T., Ding, K., Liu, L., Zhou, D., Qi, X.,  
798 and Ding, A.: Impact of Biomass Burning and Vertical Mixing of Residual-Layer Aged Plumes on  
799 Ozone in the Yangtze River Delta, China: A Tethered-Balloon Measurement and Modeling Study of  
800 a Multiday Ozone Episode, *J. Geophys. Res.-Atmos.*, 123, 11786-11803, 10.1029/2018jd028994,  
801 2018.

802 Yeatman, S. G., Spokes, L. J., Dennis, P. F., and Jickells, T. D.: Can the study of nitrogen isotopic  
803 composition in size-segregated aerosol nitrate and ammonium be used to investigate atmospheric  
804 processing mechanisms?, *Atmos. Environ.*, 35, 1337-1345, 10.1016/s1352-2310(00)00457-x, 2001.

805 Yi, Y., Meng, J., Hou, Z., Wang, G., Zhou, R., Li, Z., Li, Y., Chen, M., Liu, X., Li, H., and Yan, L.:  
806 Contrasting compositions and sources of organic aerosol markers in summertime PM(2.5 )from  
807 urban and mountainous regions in the North China Plain, *Sci. Total Environ.*, 766,  
808 10.1016/j.scitotenv.2020.144187, 2021.

809 Zhang, Y., Forrister, H., Liu, J., Dibb, J., Anderson, B., Schwarz, J. P., Perring, A. E., Jimenez, J. L.,  
810 Campuzano-Jost, P., Wang, Y., Nenes, A., and Weber, R. J.: Top-of-atmosphere radiative forcing  
811 affected by brown carbon in the upper troposphere, *Nat. Geosci.*, 10, 486-+, 10.1038/ngeo2960,  
812 2017.

813 Zheng, B., Tong, D., Li, M., Liu, F., Hong, C., Geng, G., Li, H., Li, X., Peng, L., Qi, J., Yan, L., Zhang,  
814 Y., Zhao, H., Zheng, Y., He, K., and Zhang, Q.: Trends in China's anthropogenic emissions since  
815 2010 as the consequence of clean air actions, *Atmos. Chem. Phys.*, 18, 14095-14111, 10.5194/acp-  
816 18-14095-2018, 2018.

817 Zhou, S., Wu, L., Guo, J., Chen, W., Wang, X., Zhao, J., Cheng, Y., Huang, Z., Zhang, J., Sun, Y., Fu, P.,  
818 Jia, S., Tao, J., Chen, Y., and Kuang, J.: Measurement report: Vertical distribution of atmospheric  
819 particulate matter within the urban boundary layer in southern China - size-segregated chemical  
820 composition and secondary formation through cloud processing and heterogeneous reactions,  
821 *Atmos. Chem. Phys.*, 20, 6435-6453, 10.5194/acp-20-6435-2020, 2020.

822 Zhou, Y., Hakala, S., Yan, C., Gao, Y., Yao, X., Chu, B., Chan, T., Kangasluoma, J., Gani, S., Kontkanen,  
823 J., Paasonen, P., Liu, Y., Petaja, T., Kulmala, M., and Dada, L.: Measurement report: New particle  
824 formation characteristics at an urban and a mountain station in northern China, *Atmos. Chem. Phys.*,  
825 21, 17885-17906, 10.5194/acp-21-17885-2021, 2021.

826

827

828

829

830

831 **Table caption**

832 Table 1 Mass concentrations of species in the PM<sub>2.5</sub> samples and the meteorological  
833 conditions at the two sampling sites.

834

835

836

837 **Figure captions**

838

839 Figure 1 (a) Location of the study sites in China, (b) topographic view of Mt. Hua  
840 with the sampling sites mark, and (c) vertical views of the two sampling sites and the  
841 horizontal distance between them. (The maps are produced by mapbox,  
842 <https://account.mapbox.com/>, last access, 31 Dec. 2021).

843

844 Figure 2 Time series of the temperature (T), relative humidity (RH), boundary layer  
845 height (BLH) and mass concentrations of PM<sub>2.5</sub> and the water-soluble ions in PM<sub>2.5</sub>  
846 during the observation period at the two sampling sites.

847

848 Figure 3 Diurnal variations in PM<sub>2.5</sub> and the boundary layer height (BLH) at the  
849 different observation sites.

850

851 Figure 4 Concentration-weighted trajectory (CWT) analyses of PM<sub>2.5</sub> in both the  
852 daytime (8:00-20:00) and nighttime (21:00-7:00) at the MS site.

853

854 Figure 5 The distribution of averaged diurnal divergence over the whole campaign, with  
855 corresponding wind field. (a) Horizontal distribution at surface. (b) Longitude-pressure  
856 cross-sections at 34°29'N. Wind speeds were represented by arrow sizes, and the W  
857 component of wind vectors was magnified 10 times.

858

859 Figure 6 Mass closure of PM<sub>2.5</sub> during the observed period (OM=1.6×OC).

860

861 Figure 7 Comparison of the calculated and observed NH<sub>4</sub><sup>+</sup> concentrations at the MF  
862 and MS sampling sites.

863

864 Figure 8 Schematic of the physicochemical behaviors of nitrate and ammonium during  
865 the transport process.

866

867 Figure 9 Temperature dependence of the ratio of the product of the partial pressures of  
868 NH<sub>3</sub> and HNO<sub>3</sub> with the dry dissociation constant of NH<sub>4</sub>NO<sub>3</sub>.

869

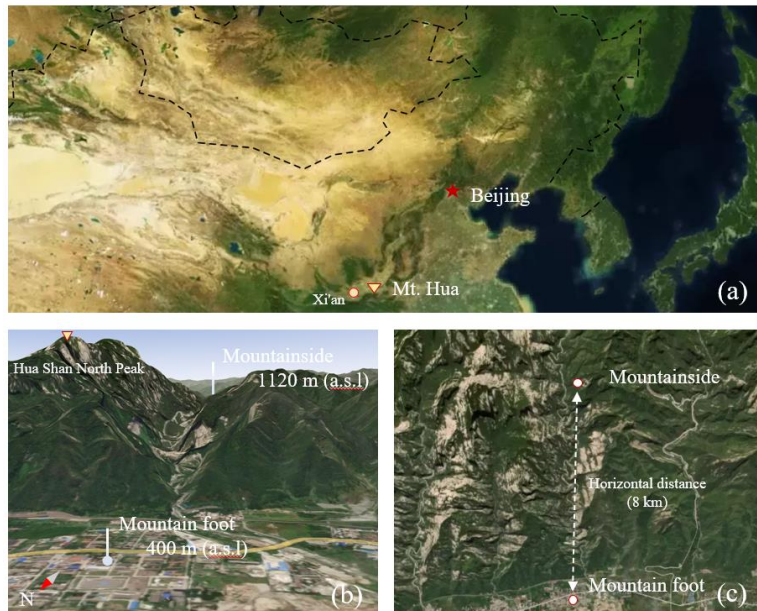
870 Figure 10 Nitrate and ammonium δ<sup>15</sup>N values at the two sampling sites in the daytime.

871  
872  
873  
874  
875  
876  
877

878 Table 1 Mass concentrations of species in the PM<sub>2.5</sub> samples, pH and the  
879 meteorological conditions at the two sampling sites.

	Mountain foot	Mountainside
<b>(i) Mass concentration of species and ALWC (µg/m<sup>3</sup>) and pH</b>		
SO <sub>4</sub> <sup>2-</sup>	10.1±6.4	9.0±7.1
NO <sub>3</sub> <sup>-</sup>	6.1±6.3	3.8±5.8
NH <sub>4</sub> <sup>+</sup>	3.9±3.3	3.9±3.5
Cl <sup>-</sup>	0.4±0.5	0.37±0.50
Na <sup>+</sup>	0.70±0.8	0.47±0.62
K <sup>+</sup>	0.2±0.3	0.37±0.5
Mg <sup>2+</sup>	0.1±0.1	0.07±0.06
Ca <sup>2+</sup>	2.5±2.0	0.9±1.2
OC	14.0±4.7	5.0±2.8
EC	4.3±2.0	1.1±0.7
PM <sub>2.5</sub>	76.0±44.1	47.0±38.0
ALWC	27.6±63.9	26.9±71.4
pH	3.4±2.2	2.9±2.0
<b>(ii) Meteorological parameters</b>		
T (°C)	23.2±4.2	15.0±2.5
RH (%)	68.9±18.2	62.8±20.0
Wind speed (m/s)	1.3±1.1	3.2±2.0
Visibility (km)	14.1±9.5	22.2±12.1

880 ALWC and pH are predicted by the thermodynamic model (E-AIM (IV))  
881



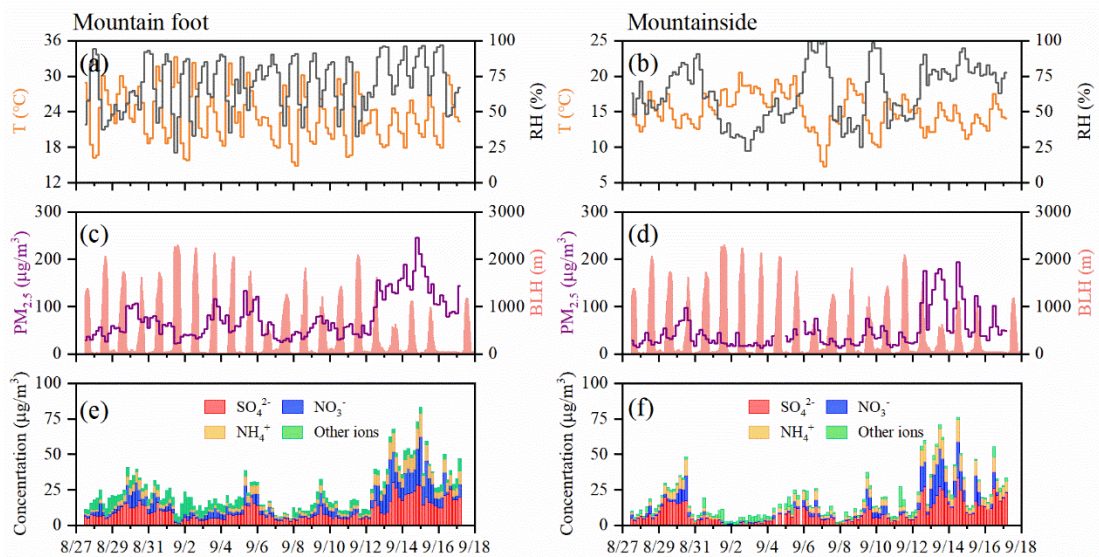
882

883 Figure 1 (a) Location of the study sites in China, (b) topographic view of Mt. Hua  
 884 with the sampling sites mark, and (c) vertical views of the two sampling sites and the  
 885 horizontal distance between them. (The maps are produced by mapbox,  
 886 <https://account.mapbox.com/>, last access, 31 Dec. 2021).

887

888

889



890

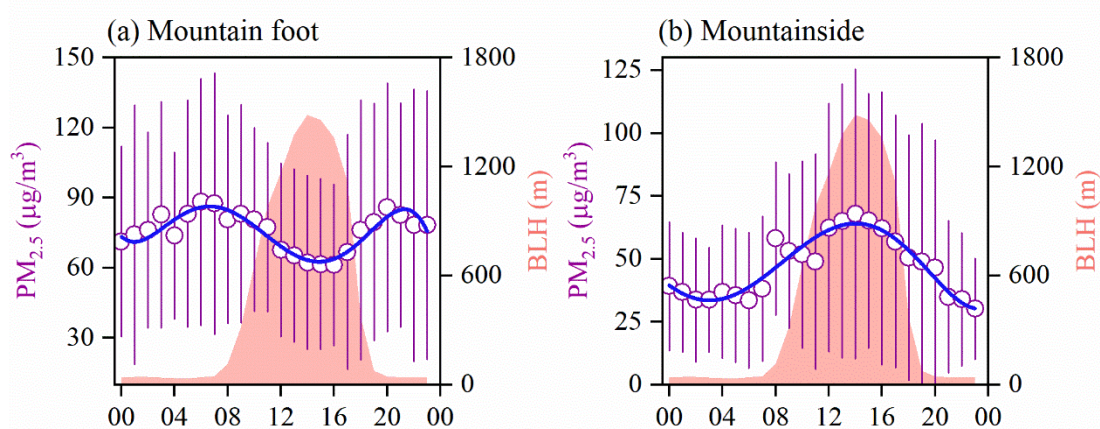
891 Figure 2 Time series of the temperature (T), relative humidity (RH), boundary layer  
 892 height (BLH) and mass concentrations of  $\text{PM}_{2.5}$  and the water-soluble ions in  $\text{PM}_{2.5}$   
 893 during the observation period at the two sampling sites.

894

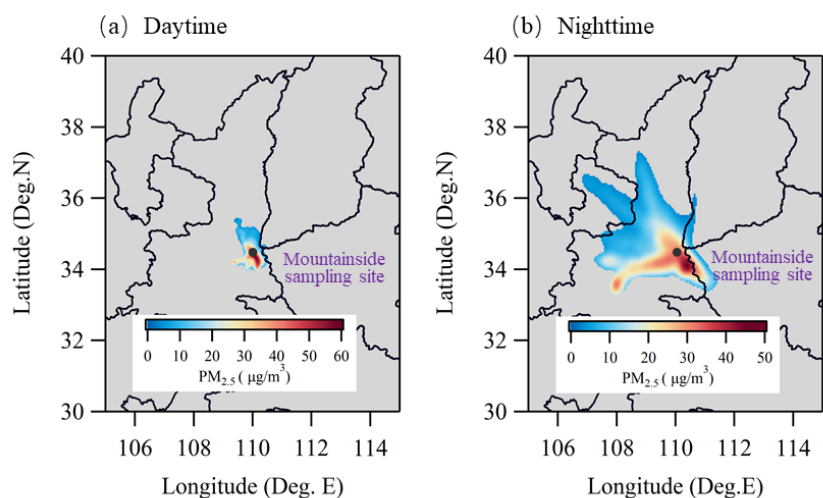
895

896

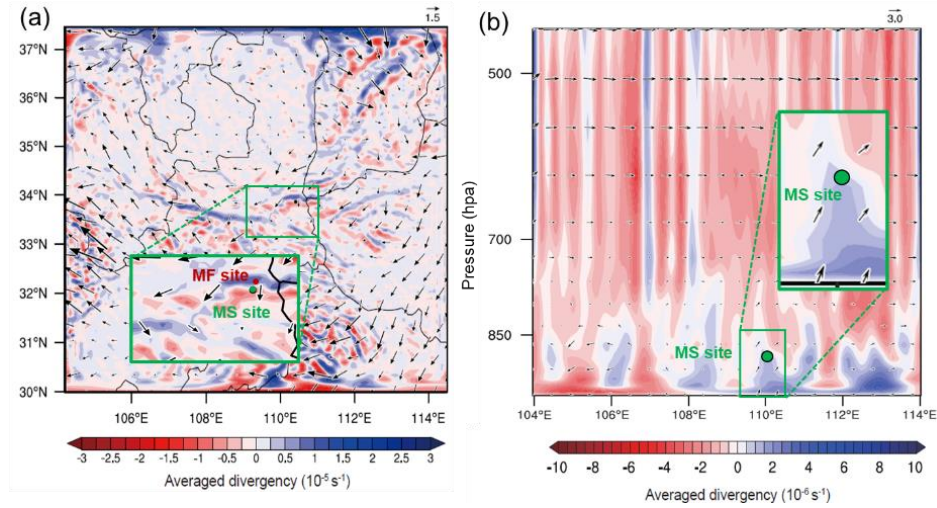
897  
898  
899  
900  
901



902  
903 Figure 3 Diurnal variations in  $PM_{2.5}$  and the boundary layer height (BLH) at the two  
904 sampling sites.  
905  
906  
907  
908  
909  
910  
911



912  
913 Figure 4 Concentration-weighted trajectory (CWT) analyses of  $PM_{2.5}$  in both the  
914 daytime (8:00-20:00) and nighttime (21:00-7:00) at the MS site.  
915  
916  
917



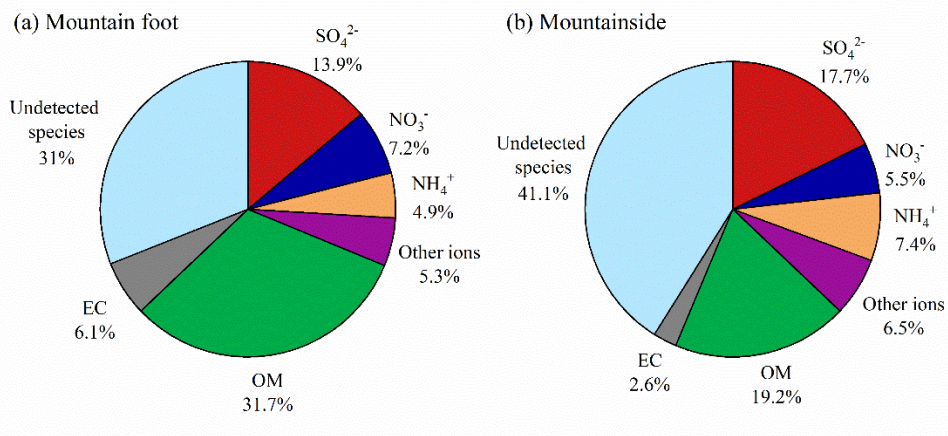
918

919

920 Figure 5 The distribution of averaged diurnal divergence over the whole campaign, with  
 921 corresponding wind field. (a) Horizontal distribution at surface. (b) Longitude-pressure  
 922 cross-sections at 34°29'N. Wind speeds were represented by arrows sizes, and the W  
 923 component of wind vectors was magnified 10 times.

924

925



926

927 Figure 6 Mass closure of  $\text{PM}_{2.5}$  during the observed period ( $\text{OM}=1.6 \times \text{OC}$ ).

928

929

930

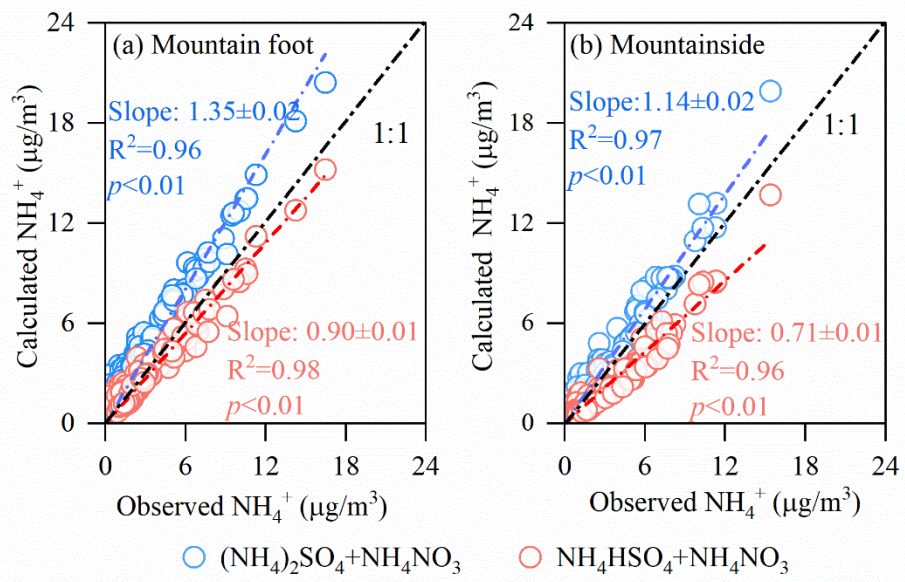
931

932

933

934

935



936

937 Figure 7 Comparison of the calculated and observed  $\text{NH}_4^+$  concentrations at both  
938 sampling sites.

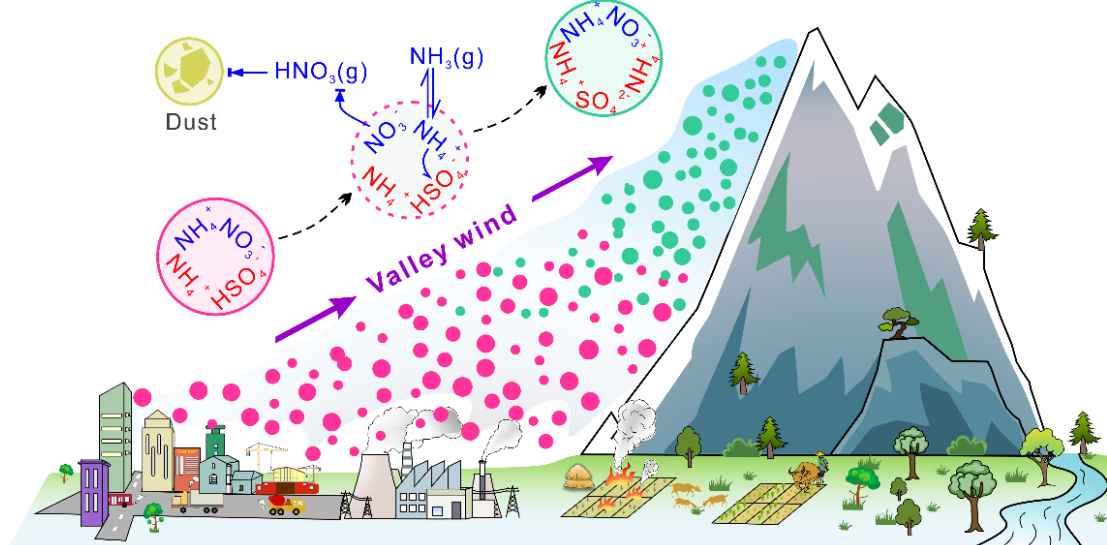
939

940

941

942

943

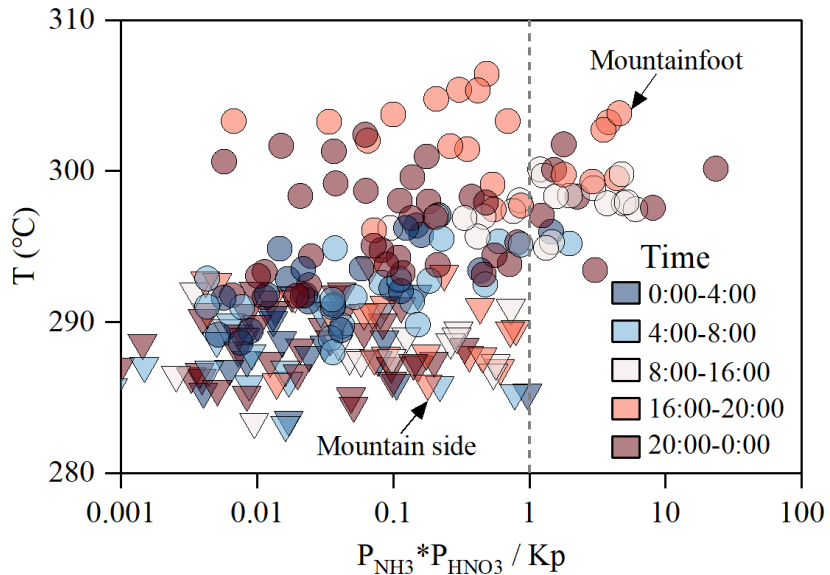


944

945 Figure 8 Schematic of the physicochemical behaviors of nitrate and ammonium during  
946 the transport process.

947

948



949

950 Figure 9 Temperature dependence of the ratio of the product of the partial pressures of  
 951 NH<sub>3</sub> and HNO<sub>3</sub> with the dry dissociation constant of NH<sub>4</sub>NO<sub>3</sub>.

952

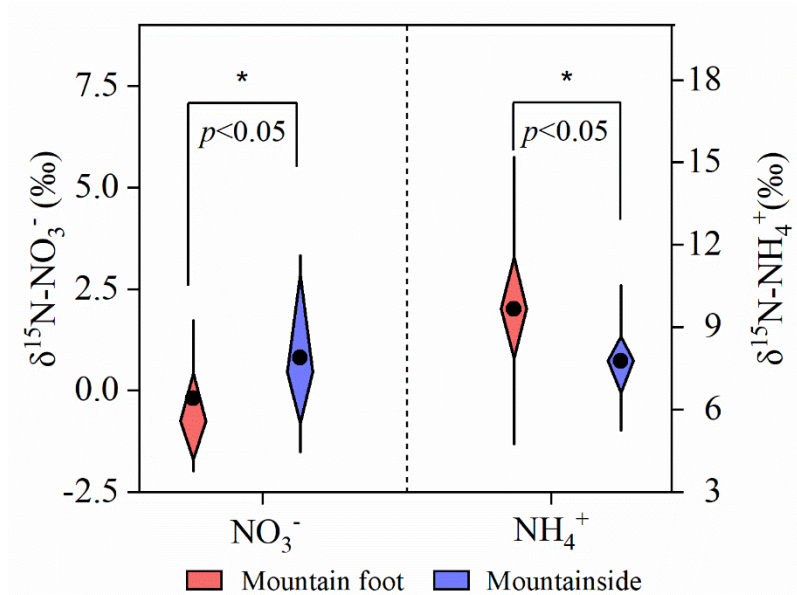
953

954

955

956

957



958

959 Figure 10 Nitrate and ammonium δ<sup>15</sup>N values at the two sampling sites in the daytime.  
 960